Zeeman and hyperfine interactions of a single $^{167}Er^{3+}$ ion in Si

Jiliang Yang,[1,3] Wenda Fan,[1,3] Yangbo Zhang,[1,3] Changkui Duan,[1,3] Gabriele G. de Boo,[4] Rose L. Ahlefeldt,[5] Jevon J. Longdell,[6] Brett C. Johnson,[7,8] Jeffrey C. McCallum,[8] Matthew J. Sellars,[5] Sven Rogge,[4] Chunming Yin,[1,2,3,*] and Jiangfeng Du[1,2,3]

[1]*CAS Key Laboratory of Microscale Magnetic Resonance and School of Physical Sciences, University of Science and Technology of China, Hefei 230026, China*

[2]*Hefei National Laboratory, Hefei 230088, China*

[3]*CAS Center for Excellence in Quantum Information and Quantum Physics, University of Science and Technology of China, Hefei 230026, China*

[4]*Centre of Excellence for Quantum Computation and Communication Technology, School of Physics, University of New South Wales, NSW 2052, Australia*

[5]*Centre of Excellence for Quantum Computation and Communication Technology, Research School of Physics, Australian National University, ACT 0200, Australia*

[6]*The Dodd-Walls Centre for Photonic and Quantum Technologies, Department of Physics, University of Otago, Dunedin 9016, New Zealand*

[7]*Centre of Excellence for Quantum Computation and Communication Technology, School of Engineering, RMIT University, Victoria 3001, Australia*

[8]*Centre of Excellence for Quantum Computation and Communication Technology, School of Physics, University of Melbourne, Victoria 3010, Australia*

(Received 21 April 2022; revised 16 June 2022; accepted 16 June 2022; published 27 June 2022)

Er-doped Si is a promising candidate for quantum information applications due to its telecom wavelength optical transition and its compatibility with Si nanofabrication technologies. Recent spectroscopic studies based on photoluminescence excitation have shown multiple well-defined lattice sites that Er occupies in Si. Here we report a measurement of the Zeeman and hyperfine tensors of a single $^{167}Er^{3+}$ ion in Si. All the obtained tensors are highly anisotropic with the largest value principal axes aligning in nearly the same direction, and the trace of the lowest crystal field level **g**-tensor is 17.78 ± 0.40. The results indicate that this specific Er site is likely to be a distorted cubic site that exhibits monoclinic (C_1) symmetry. Finally, zero first-order-Zeeman fields are identified for this site and could be used to reduce decoherence of hyperfine spin states in future experiments.

DOI: 10.1103/PhysRevB.105.235306

I. INTRODUCTION

Er^{3+} ions have been widely used in classical optical devices and networks thanks to the $^4I_{15/2}$ - $^4I_{13/2}$ optical transition at telecom wavelength. Recent studies on Er^{3+} ions have demonstrated new prospects for quantum optics and quantum computing with direct optical access to telecom fiber networks and Si photonic cavities. Er^{3+} is particularly attractive for quantum applications because of the long coherence time available on hyperfine or electronic spin states. For example, hyperfine coherence time can exceed 1 s for Er^{3+} ions in Y_2SiO_5 [1] and a 23 ms electron spin coherence time has been demonstrated for Er^{3+} ions in a natural-abundance crystal, $CaWO_4$ [2]. Further enhancement can be achieved by utilizing hyperfine transitions at a zero first-order-Zeeman (ZEFOZ) field that are protected from magnetic field fluctuations [3]. In addition, strong cavity coupling and coherent control of a single Er^{3+} ion have been demonstrated by combining a Si cavity with an Er-doped Y_2SiO_5 crystal [4,5].

Si would be an obvious choice of host materials for Er^{3+} ions due to the well-established Si nanofabrication technologies. Also, the nuclear-spin free environment provided by isotopically purified ^{28}Si can significantly suppress decoherence due to nuclear spins in the host crystal. One challenge is that Er^{3+} ions can form a range of sites in Si in contrast to only two crystallographic sites that Er^{3+} ions occupy in Y_2SiO_5 [6]. By choosing a suitable annealing condition and Er concentration, a cubic Er site can become the dominant site in float-zone Si with low impurity levels [7]. The typical structure of its photoluminescence (PL) spectra includes an optical transition at 195.01 THz between its lowest levels of the $^4I_{15/2}$ and $^4I_{13/2}$ states. While complex spectra appear in Er-doped Si under different annealing conditions or in the presence of other dopants or implantation-induced defects [8], the spectral structure of this cubic site is still observable. Analysis of the fine structure suggests the Er^{3+} ion sees a tetrahedral crystal field [7,9]. Also, existence of a tetrahedral interstitial Er site in Si was confirmed by emission channelling studies [10], although there was no direct experimental link between this result and earlier measurements. These findings are in agreement with several theoretical studies that the tetrahedral interstitial site is the most stable site for Er in Si [11–14], but other studies found a tetrahedral substitutional site [15,16] to be more stable or a hexagonal interstitial site when oxygen is involved [12,15].

*Chunming@ustc.edu.cn

The most direct evidence of a cubic site would be an isotropic Zeeman **g** tensor, but the **g** tensor of the cubic Er site in Si has not been determined due to the complex spectra and limited resolution from PL or electron paramagnetic resonance measurements. Another characteristic property is the trace of the Z_1 **g** tensor, where Z_1 represents the lowest crystal field level of the $^4I_{15/2}$ ground state. Crystal-field levels of a cubic site can be either Γ_8 quartet states or doublet states of Γ_6 or Γ_7, but only Γ_6 and Γ_7 Z_1 levels have been experimentally identified in Er-doped crystals [17]. The trace of the Z_1 **g** tensor for Γ_6 and Γ_7 is calculated to be 20.4 and 18.0 based on crystal field theory, and the measured values in two cubic crystals are on average 20.27 ± 0.12 and 17.79 ± 0.03, respectively [17]. The small deviation from the calculated value is usually explained by interactions with higher-lying energy levels or the effects of covalency [18,19]. Er^{3+} ions can also occupy a slightly distorted cubic site where the crystal field distortion is small compared to the cubic crystal field. As a result, the distortion on the trace of the Z_1 **g** tensor is expected to be smaller than 0.3 [19] and the cubic crystal field approximation is still valid [20].

Recent high-resolution photoluminescence excitation (PLE) measurements on Si waveguides [22,23] and bulk Si [24] have both shown multiple well-defined Er sites. The inhomogeneous linewidths are of the order of 1 GHz, which is comparable to that of Er^{3+} :Y_2SiO_5, and some sites show homogeneous linewidths below 1 MHz. These studies reinforce the promise of Er in Si, but for applications where long coherence times are required, extensive studies of the Zeeman and hyperfine interactions of the Er sites in Si are also required. The Zeeman interaction defines the preferred magnetic field direction to suppress electron spin relaxation due to spin-lattice coupling. Further, hyperfine transitions at a ZEFOZ field are protected from magnetic field fluctuations and thus allow extended spin coherence times [25]. The Zeeman splitting can be observed for some Er sites using PLE, but the resolution is limited by the ∼1 GHz inhomogeneous linewidth and may be further limited by multiple site orientations [24].

The inhomogeneous broadening can be avoided by looking at only one ion. The hybrid electrical/optical single ion detection enables the high spectral resolution study of the Zeeman and hyperfine interactions on a single ion level [26,27]. Recently, a time-resolved single ion detection technique was demonstrated [21] by detecting the ionization of a single trap as opposed to multiple traps in the previously used time-averaged measurements [26,28]. The time-resolved detection has the advantage of allowing a wider range of experimental conditions and faster repetition of the single ion detection than the time-averaged detection [21]. While the earlier studies with time-averaged detection revealed a large number of optical transitions from 193.5 THz to 197.0 THz [24], optical transitions at approximately 195.04 THz are frequently observed in devices showing single trap ionization with and without oxygen co-implantation, as shown in Table I.

Here we investigate the Zeeman and hyperfine interactions of a single $^{167}Er^{3+}$ ion in Si. This Er site has a zero-field optical transition frequency of 195036.7 GHz (1537.107 nm) which closely matches the previously reported cubic site in Si [7]. A spin Hamiltonian model is used to fit the spectra from field rotation measurements. The fitting gives the Zeeman interaction **g** tensors and the hyperfine interaction **A** tensors for the lowest crystal field level in the $^4I_{15/2}$ manifold and a crystal field level in the $^4I_{13/2}$ manifold of the $^{167}Er^{3+}$ ion.

TABLE I. List of devices in which Er^{3+} transitions were observed by detecting the ionisation of a single trap.

Device	Transitions (THz)	Note
1(Er)	194.05, 195.03 195.07, 196.02	
2(Er+O)	195.03	
3(Er+O)	195.04, 195.94	
4(Er+O)	195.04, 195.99	The present paper
5(Er+O)	195.07	
6(Er+O)	195.12	
7(Er+O)	195.15	
8(Er+O)	195.35	Ref. [21]

II. SPIN HAMILTONIAN MODEL

Er forms a trivalent state in most semiconductors with a $4f^{11}$ electronic configuration. The telecom wavelength optical transitions arise from the $^4I_{15/2}$ ground-state multiplet and the $^4I_{13/2}$ first optically excited state. Under the action of a crystal field, the $2J + 1$ degeneracy in these levels is partially or wholly lifted. For example, the $^4I_{15/2}$ state splits into five levels for the special case of the cubic site and eight levels for low-symmetry sites.

Figure 1(a) shows a generic energy level diagram of the low-symmetry Er site investigated in this paper. The crystal field levels of $^4I_{15/2}$ ($^4I_{13/2}$) are labeled as Z_1 up to Z_8 (Y_1 up to Y_7) in order from the lowest energy to the highest. For a low-symmetry site, the electron and nuclear spin quantum numbers are not necessarily good and in general do not refer to the same directions in the ground and excited states. Here, an effective spin model with $S = 1/2$ and $I = 7/2$ is used to describe the system. Each crystal-field level has a twofold electron spin degeneracy (Kramers doublet) which can be lifted by a magnetic field. For a $^{167}Er^{3+}$ ion with a nuclear spin of $I = 7/2$, each crystal field doublet splits into 16 hyperfine sublevels. The Zeeman and hyperfine splittings of a crystal-field level can typically be described in low field by a spin Hamiltonian [6,29,30],

$$H = \mu_e \mathbf{B} \cdot \mathbf{g} \cdot \mathbf{S} + \mathbf{I} \cdot \mathbf{A} \cdot \mathbf{S} + \mathbf{I} \cdot \mathbf{Q} \cdot \mathbf{I} - \mu_n g_n \mathbf{B} \cdot \mathbf{I}, \quad (1)$$

where **B** is the external magnetic field, **S** is an effective spin vector, **I** is a nuclear spin vector, **g**, **A**, and **Q** are the Zeeman, hyperfine, and quadrupole tensors, μ_e and μ_n are the Bohr and nuclear magneton, respectively, and $g_n \sim -0.1618$ is the nuclear g factor.

At liquid helium temperatures, only the lowest crystal-field level Z_1 is populated, and optical transitions between Z_1 and multiple crystal field levels Y_i can be observed. When the electronic Zeeman splitting is much larger than the hyperfine splitting, the transitions between Z_1 and Y_i can be split into four transition groups *a,b,c,d* as shown in Fig. 1(a). The four transition groups are well separated in transition frequency,

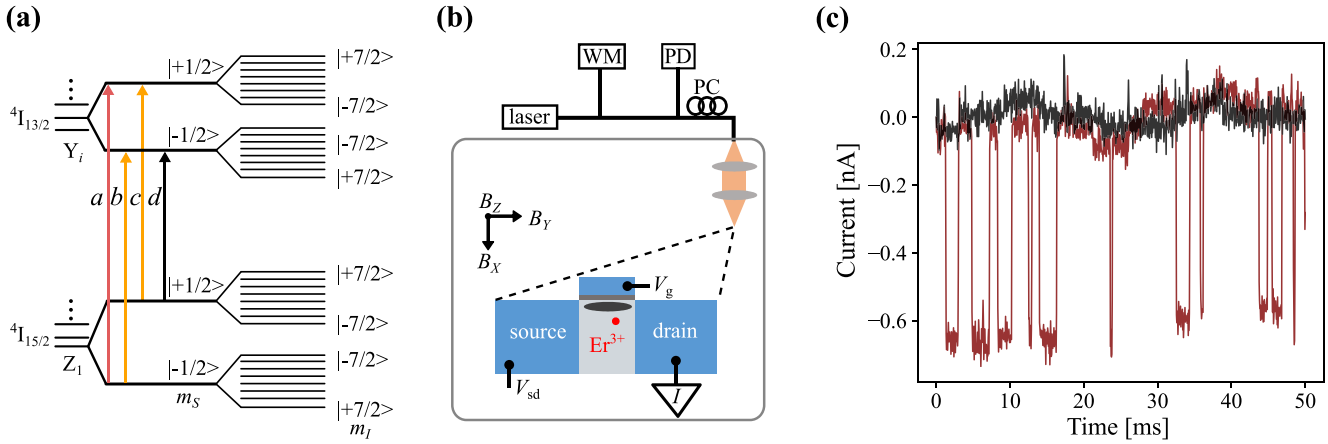

FIG. 1. Spectroscopic measurement of a $^{167}Er^{3+}$ ion. (a) A generic energy-level diagram of a $^{167}Er^{3+}$ ion in a high magnetic field. m_S and m_I represent the spin projection quantum numbers of the electronic and hyperfine spin states, respectively. (b) A schematic of the FinFET device and its electrical and optical connections. The laser beam is focused on the channel region of the device doped with $^{167}Er^{3+}$ ions. (c) Two typical current-time traces measured under resonant (red) and nonresonant (black) illumination.

and each group contains eight hyperfine spin preserving peaks with $\Delta m_I = 0$. When the Zeeman splitting and hyperfine splitting become comparable, hyperfine sublevels from different Zeeman branches start to mix.

III. SETUP AND SPECTROSCOPY

The experimental setup and the device used in this work are illustrated in Fig. 1(b). The device was a Si fin-field-effect transistor (FinFET) consisting of three terminals and a nanowire channel (35 nm width × 80 nm length × 60 nm height). ^{167}Er and O were implanted into the device followed by a 700 °C annealing to repair the implantation damage. The estimated concentration of Er and O in the channel is 1×10^{17} cm^{-3} and 1×10^{18} cm^{-3}, respectively. Additionally, the p-type channel had a B doping concentration of 3×10^{18} cm^{-3}. The device was installed on the cold stage of a liquid helium-free cryostat operating at a base temperature of 3.6 K. The cryostat is equipped with a 6-1-1 T superconducting vector magnet, which can provide a magnetic field up to 1 T in any direction. The device was placed at the center of the magnet, and the field homogeneity is for the X and Y axes and 0.1% for the Z axis over a 1 cm diameter of spherical volume.

A fiber-coupled frequency-tunable laser (Pure Photonics PPLC550) was used to excite the optical transitions. The laser light was split into two beams. One beam was sent to a photodetector (PD) and a wavemeter (WM) for power and wavelength monitoring. The specified repeatability of the wavemeter (Bristol 621A-NIR) is ±6 MHz. The other beam went through a polarization controller (PC) and optical fibers and reached the cold stage. The light was focused onto the device surface by a two-lens objective [31] and the spot size was approximately 2 μm.

Single Er^{3+} ion spectra were measured with an optical-electrical hybrid method [21,26]. The FinFET was biased under a subthreshold gate voltage [32] so single quantum dots (QDs) form in the device channel. These QDs can work as sensitive charge sensors and detect the loss or gain of a single electron in its vicinity. After the Er^{3+} ion was excited into the $^4I_{13/2}$ excited state by resonant light, it would relax back to the $^4I_{15/2}$ ground state via either a radiative process by photon emission or nonradiative processes.

Our previous studies have demonstrated that a nonradiative relaxation of an Er^{3+} ion can cause a nearby trap to ionise [21], and afterward, the trap resets by capturing an electron. These processes can be seen from a typical current-time trace (red) in Fig. 1(c) measured under resonant illumination. The current through the QD switches between two discrete levels due to ionisation and reset events. In contrast, the black current-time trace was measured with a nonresonant laser frequency and the current stays at the background level. The spectra presented in this paper were measured under continuous wave laser excitation and the spectral signal was defined as the number of ionisation events per unit time per unit power in a long current-time trace. In principle, a longer current-time trace gives a more accurate spectral signal at each frequency, and a finer frequency step size leads to more data points for the peak fitting, but both will lead to longer measurement times. Therefore, a trade-off was made between these two parameters, and a frequency step size of 20 MHz and a trace length of 5 s were used in this paper.

IV. FIELD ROTATION MEASUREMENT

To determine the anisotropic spin Hamiltonian tensors, we used the vector magnet to apply fields along different directions while holding the field magnitude fixed at 0.4 T. For a low-symmetry site, high anisotropy is expected for the **g** tensors, and resonant frequencies of the four transition groups vary considerably as the field rotates. Therefore, we started with a preliminary measurement to determine a simplified spin Hamiltonian with only the electronic Zeeman term, which can be used to identify a suitable laser frequency scanning range for each field direction. First, the four transition groups were measured by rotating the field in a circle within the three orthogonal planes (XOY, YOZ, ZOX) of the laboratory frame. Second, spectral scans were performed in high magnetic fields along the Z axis to identify the ground electron

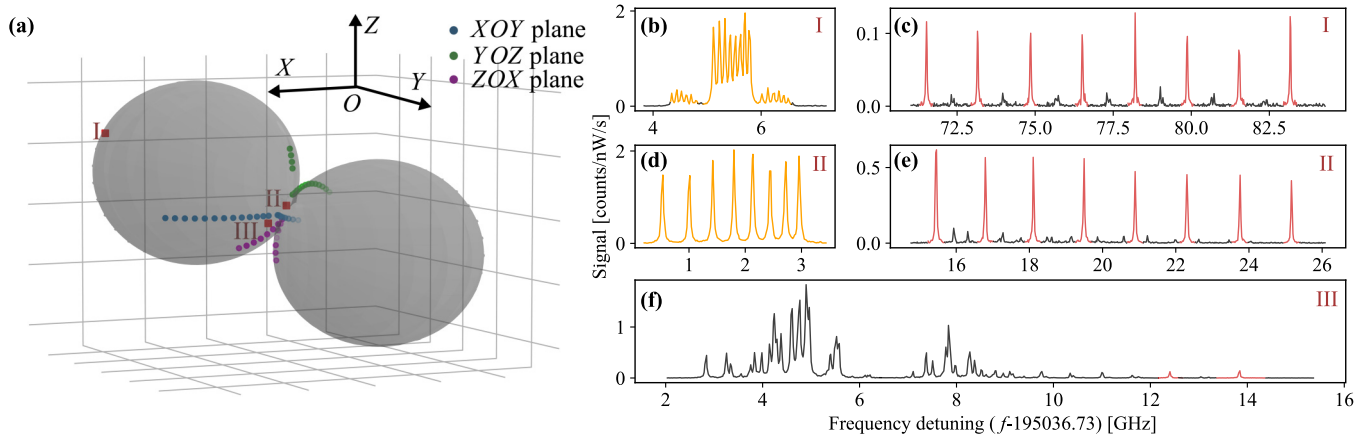

FIG. 2. Field rotation Zeeman spectroscopy. (a) A subset of the selected magnetic field directions. The peanut shape contour shows the Zeeman splitting amplitudes of the Z_1 level when the magnetic field points in different directions and the colored dots on the contour surface denote the selected field directions. Each dot indicates a magnetic field vector direction from the origin O to the dot, and its color is used to highlight different groups of directions and its brightness comes from the 3D lighting effect. Three sets of spectra are shown as examples in (b)–(f), and the Roman numeral on the top right corner of each figure denotes the magnetic field direction in use and corresponds to the Roman numerals in (a). The colored spectral peaks in (b)–(f) were used for the spin Hamiltonian fitting.

spin level of Z_1 and to assign the *a,b,c,d* optical transition groups to the corresponding Z_1 and Y_i electron spin levels. In addition, the results suggest that the measured Y_i level is likely to be the Y_1 level. (See Appendix B for details.) Finally, the fitting results gave the Z_1 and Y_i **g** tensors, and both turned out to be highly anisotropic with similar orientation.

The preliminary **g** tensors were then used to select the directions for the field rotation measurement. The peanut shape contour in Fig. 2(a) shows the Zeeman splitting amplitudes of the Z_1 level when the magnetic field is along different directions, and the colored dots on the contour surface denote a subset of the selected field directions while the full set can be found in the Supplemental Material [33]. Each dot indicates a magnetic field vector direction from the origin O to the dot and its color is used to highlight different groups of directions and its brightness comes from the 3D lighting effect.

To help the understanding of the field direction selection strategy, three sets of spectra are shown as examples in Figs. 2(b)–2(f). Only the spectral peaks that can be properly assigned to energy levels and show good peak contrast were used for the final spin Hamiltonian fitting, such as the orange and red spectral peaks in Figs. 2(b)–2(f). Multipeak fitting with Lorentzian functions was used to determine the peak positions. The full width at half maximum of the isolated peaks was approximately 32 MHz [34]. Since the spectra were measured with a finite step size of 20 MHz, the apparent peak heights in Figs. 2(b)–2(f) show arbitrary fluctuations and the highest points do not necessarily correspond to the fitted peak heights or center frequencies.

The two ends of the peanut shape contour in Fig. 2(a) correspond to the principal axis of the **g** tensor with the largest **g** value, defined as g_z. A typical set of spectra in this region is shown in Figs. 2(b) and 2(c) and its field direction is denoted by the red square I in Fig. 2(a). Specifically, Fig. 2(b) shows the transition group *b* which comprises eight strong hyperfine peaks corresponding to $\Delta m_I = 0$ in the central region and two sets of seven weaker hyperfine peaks corresponding to $|\Delta m_I| = 1$ in the two side regions. Figure 2(c) shows the transition group *a* with a lower overall signal than group *b*. Group *a* also consists of eight stronger $\Delta m_I = 0$ peaks but the weaker $|\Delta m_I| = 1$ peaks distribute between the $\Delta m_I = 0$ peaks. These features show up similarly when the magnetic field points in most directions except the waist region of the peanut shape contour, where the two transverse principal axes lie, with smaller **g** values, defined as g_y and g_x. In this transverse field region, the Zeeman splitting becomes comparable to the hyperfine splitting. Some $|\Delta m_I| = 1$ and $\Delta m_I = 0$ hyperfine peaks start to overlap, and some $|\Delta m_I| = 1$ peaks become stronger due to the mixing of spin states. These phenomena can be seen from spectra II and III in Figs. 2(d)–2(f), and the field directions are denoted by the red squares II and III in Fig. 2(a), respectively.

In total, 181 different field directions were selected into two categories. One category covers the entire space as the magnetic field follows a three-dimensional (3D) spiral path. These field directions can be seen in the Supplemental Material [33] and three of them are denoted by the red squares in Fig. 2(a). The other category focuses on the transverse field region with three field rotational scans within the three orthogonal planes (XOY, YOZ, ZOX) of the laboratory frame, as indicated by the blue, green, and purple dots in Fig. 2(a). The spectral information in this region is critical for improving the fitting accuracy of the smaller values in the Zeeman and hyperfine tensors. Due to the level mixing and anticrossing in this region, intensities of transitions become equivalent and hyperfine peaks are unevenly spaced, as can be seen in spectra II and III [29].

V. SPIN HAMILTONIAN FITTING

Using the method described above, 5788 hyperfine transition peaks were identified from the 181 spectral scans and were used for the spin Hamiltonian fitting. For a low-symmetry Er site, the principal axes of the **g**- and **A**-tensors of different crystal field levels may deviate from each other. Therefore, each tensor has six independent variables, i.e.,

TABLE II. Principal values and Euler angles for all tensors.

	Principal values	Euler angles (deg)
	$g_z = 14.846 \pm 0.028$	$\alpha = 137.50 \pm 0.13$
	$g_y = 2.38 \pm 0.18$	$\beta = -66.036 \pm 0.099$
	$g_x = 0.55 \pm 0.19$	$\gamma = -155.7 \pm 2.0$
$Z_1(^4I_{15/2})$	$A_z = 1.558 \pm 0.019$	$\alpha = 138.8 \pm 4.8$
	$A_y = 0.56 \pm 0.21$ (GHz)	$\beta = -66.3 \pm 6.9$
	$A_x = 0.30 \pm 0.16$	$\gamma = -65 \pm 47$
	$g_z = 13.100 \pm 0.023$	$\alpha = 129.74 \pm 0.11$
	$g_y = 0.59 \pm 0.17$	$\beta = -71.87 \pm 0.11$
	$g_x = 0.16 \pm 0.16$	$\gamma = -161 \pm 25$
$Y_i(^4I_{13/2})$	$A_z = 1.773 \pm 0.023$	$\alpha = 127.4 \pm 6.6$
	$A_y = 0.42 \pm 0.14$ (GHz)	$\beta = -72.2 \pm 7.5$
	$A_x = 0.07 \pm 0.16$	$\gamma = -101 \pm 55$

three principal values and three Euler angles. Euler rotations followed a $z - y' - z''$ sequence. A diagonal matrix $\mathbf{M_p}$ defined in the coordinate system of the principal axes (x, y, z) can be transformed to a matrix $\mathbf{M}$ defined in the laboratory frame (X, Y, Z) by the following relation:

$$\mathbf{M} = \mathbf{R}^{\mathbf{T}} \cdot \mathbf{M_p} \cdot \mathbf{R}, \tag{2}$$

where $\mathbf{R} = \mathbf{R}_{z''}(\gamma) \cdot \mathbf{R}_{y'}(\beta) \cdot \mathbf{R}_z(\alpha)$, and $\mathbf{R}_i$ represents a rotation matrix of an angle (α, β, or γ) about the axis i. Here y', z'' are the new axes after the first and second rotations.

In principle, the quadrupole interaction term $\mathbf{Q}$ can be determined by the field rotation Zeeman experiment. However, its most significant impact on the identifiable spectral peaks was found to be smaller than 10 MHz. This impact could not be measured accurately due to the ±6 MHz repeatability of the wavemeter. Therefore, the quadrupole interaction term was not included in the fitting. The final spin Hamiltonian model includes 12 free parameters for each of the Z_1 and Y_i levels and another free parameter for the optical transition frequency. The Hamiltonian fitting used a global optimisation technique, basin-hopping, to minimize the root-mean-square deviation (rmsd) calculated from the residuals as follows:

$$\text{rmsd} = \sqrt{\frac{1}{N}\sum_{k=1}^{N}\left(f_k^{\text{exp}} - f_k^{\text{sim}}\right)^2}, \tag{3}$$

where f_k^{sim} and f_k^{exp} are the simulated and measured center frequency of spectral peak k, and N is the total number of peaks in the fitting.

The fitting gives an rmsd value of 83 MHz. Table II shows the fitting parameters. Only absolute values are quoted for the principal values. All four tensors are highly anisotropic, with one principal value (g_z) much larger than the other two (g_y and g_x), consistent with low site symmetry. The misalignment between the Z_1 and Y_i **g** tensors indicates that the Er site has monoclinic (C_1) symmetry.

The previously reported cubic Er site in Si has an optical transition frequency of 195.01 THz [7], which closely matches the C_1 Er site in the present paper. Also, the trace of Z_1 **g** tensor is 17.78 ± 0.40, which matches the expected value for a Γ_7 Z_1 state. This match reveals that the cubic crystal field approximation holds for this C_1 Er site in Si [19,20]. Overall, these properties suggest that this C_1 Er site is likely to be a distorted cubic site. Parameter uncertainties in Table II are calculated using the Markov chain Monte Carlo sampling method. The four tensors' largest principal values (g_z, A_z) have smaller uncertainties than the transverse principal values (g_y, g_x, A_y, A_x) due to the challenges associated

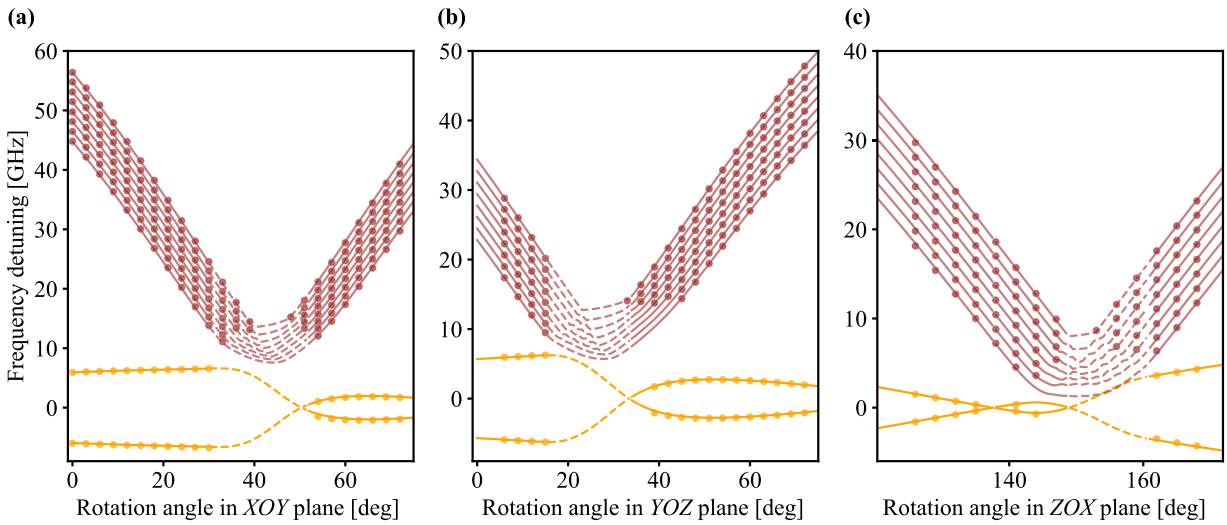

FIG. 3. Field rotation measurement results and fittings within the three orthogonal planes of the laboratory frame. Measured (colored dot) and calculated (colored line) spectral peak positions are plotted as a function of the field rotation angle as the magnetic field rotates within (a) XOY plane, (b) YOZ plane, and (c) ZOX plane. Red dots and lines correspond to the eight $\Delta m_I = 0$ transitions in group a. Orange dots and lines correspond to groups b and c. Since the spacing between adjacent hyperfine peaks in groups b and c is too small to be presented together with group a, only the fourth lowest energy transition among the eight $\Delta m_I = 0$ hyperfine transitions of group b (and c) is plotted. Due to state mixing in the anticrossing regions, the calculated $\Delta m_I = 0$ transitions may become weaker than other transitions, e.g., $|\Delta m_I| = 1$, so dashed lines are used in these regions.

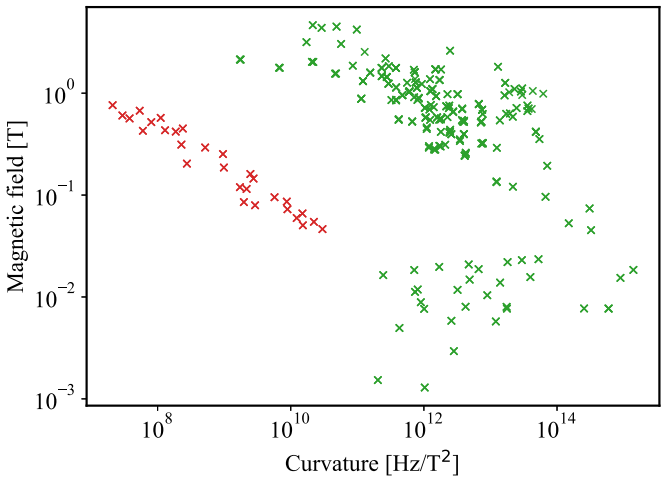

FIG. 4. Field strength vs the maximum curvature of the ZEFOZ fields found for the $^{167}Er^{3+}$ ion. The red and green points correspond to ZEFOZ fields in weakly and strongly mixed regimes, respectively.

with the high anisotropy of the tensors. First, the electron spin quantization axis $\hat{\mathbf{n}} = \mathbf{B}\cdot\mathbf{g}/(|\mathbf{B}\cdot\mathbf{g}|)$ remains close to the z direction for a wide range of field directions as a result of the high anisotropy of the **g** tensor, except in the transverse field region. This means that the transverse field region is critical for determining the transverse principal values, g_y and g_x; however, only a limited number of spectral peaks can be identified in this region due to spin mixing. Second, the hyperfine splitting is similarly impacted by the high anisotropy of both **A** and **g** tensors, as primarily determined by $|\mathbf{A}\cdot\hat{\mathbf{n}}|$ [6]. Overall, the uncertainties may be underestimated because of the large number of fitting parameters [6]. In addition, the final position of the device may change slightly during cooldown due to thermal expansion and contraction, and consequently, the actual magnetic field at the Er^{3+} ion might deviate from the set field especially for X and Y axes because of the field inhomogeneity.

To evaluate the fitting in the transverse field region, measured and calculated spectral peak positions of groups *a,b,c* from the three in-plane field rotation scans are presented in Fig. 3. The eight red spectral lines in the upper sections of Figs. 3(a)–3(c) correspond to the eight calculated $\Delta m_I = 0$ hyperfine transitions of group a, and the red dots represent the measured peaks that can be identified and were used for fitting. The spacing between adjacent hyperfine peaks in groups b and c is much smaller than group a. For clarity, then, only the fourth lowest energy transition among the eight $\Delta m_I = 0$ hyperfine transitions of group b (and c) is plotted in Fig. 3, and the orange dots and lines represent the measured and calculated peak positions, respectively.

In the region where electronic and hyperfine spins are highly mixed, spectral peaks are generated between sorted hyperfine levels in the Z_1 and Y_i states similar to hyperfine transitions outside this region. Due to state mixing, these calculated transitions may become weaker in the anticrossing region, so dashed lines are used in this region.

The four tensors have very similar α and β Euler angles, which determine the direction of the z principal axes of the four tensors. The similarly orientated **A** and **g** tensors lead to nearly identical hyperfine spectra outside the transverse field region, similar to spectrum I in Fig. 2(b). This phenomenon can also be seen from the left parts of Figs. 3(a) and 3(c), even though the three scans in Fig. 3 focus on the transverse field region.

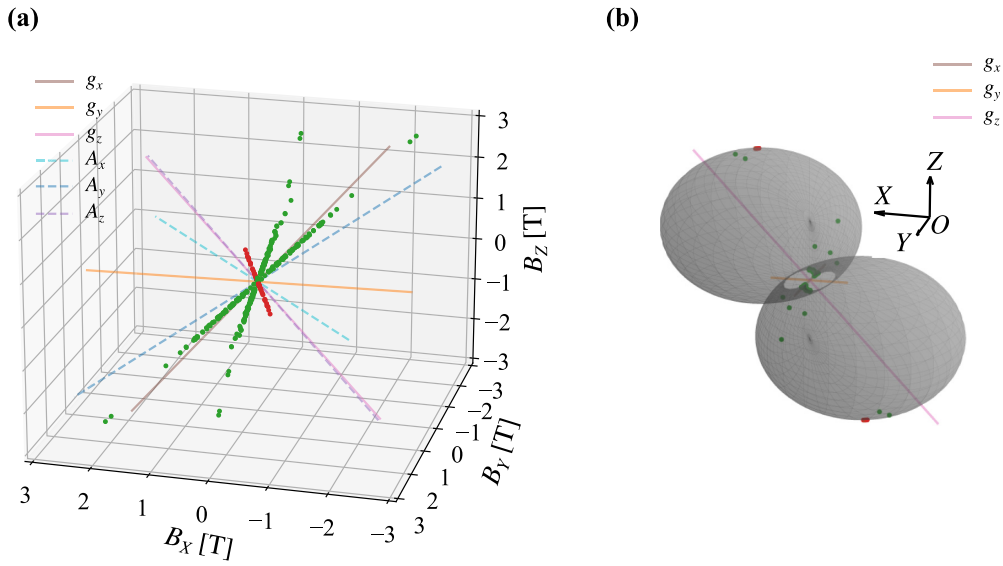

FIG. 5. 3D view of the ZEFOZ fields with a field strength below 5 T. (a) ZEFOZ field vectors. Each colored dot represents a ZEFOZ field vector, and the red and green points represent ZEFOZ fields in weakly and strongly mixed regimes, respectively. The colored solid and dashed lines indicate the directions of the principal axes of the Z_1 level **g** tensor and **A** tensor, respectively. (b) Directions of the ZEFOZ fields. The peanut shape contour shows the Zeeman splitting amplitudes of the Z_1 level when the magnetic field points in different directions. The colored dots on the contour surface denote the field directions, and each dot indicates a magnetic field vector direction from the origin O to the dot.

To locate the ZEFOZ fields for the $^{167}Er^{3+}$ ion, we follow the calculation procedures described in Ref. [25] using the fitting results. The hyperfine spin transitions between any two of the sixteen hyperfine sublevels of Z_1 are considered in the calculation. The curvatures at all ZEFOZ fields are calculated and plotted into two groups (red and green) in Fig. 4. The red group contains field directions close to the largest value principal axis of the Z_1 **g** tensor. This is a weakly mixed regime, where the electronic Zeeman term dominates and the electron spin is close to a good quantum number. ZEFOZ fields of the green group are either in the transverse field region of the peanut shape contour or so weak that the electronic Zeeman splitting is smaller than or comparable to the hyperfine splittings. Due to the state mixing, ZEFOZ transitions in this strongly mixed regime tend to have stronger transition strengths than those in the weakly mixed regime. Furthermore, these ZEFOZ fields cluster around particular directions, as shown in Fig. 5, and additional figures of the ZEFOZ fields can be found in Appendix C.

The decoherence rate induced by magnetic noise at ZEFOZ fields can be estimated as $S_2(\Delta B)^2$, where S_2 is the curvature of ZEFOZ transition and ΔB is the magnetic field fluctuation. To give an estimation on the decoherence, we consider an experimental condition of sub-Kelvin temperatures and 1 T magnetic fields, which can be provided in commercial vector magnet cryogenic systems. The magnetic field fluctuations experienced by $^{167}Er^{3+}$ ions in natural Si are dominantly due to the flipping of nearby ^{29}Si nuclear spins and other Er^{3+} electron spins. From Monte Carlo simulations [35], ΔB for an Er doping concentration of $1 \times 10^{17}\,cm^{-3}$ in natural Si is dominated by the flipping of ^{29}Si nuclear spins and is estimated to be 0.01 mT. The results suggest that $^{167}Er^{3+}$ spin coherence times in ZEFOZ fields of about 1 T in natural Si can potentially reach 1 s in the strongly mixed regime and 1 min in the weakly mixed regime. The estimation is indicative and decoherence suppression is also expected from the frozen core effect [1,36,37], as the moderate field and low temperature considered here can freeze most electron spins in the crystal.

VI. CONCLUSION

We investigated the Zeeman and hyperfine interactions of the lowest crystal-field level Z_1 in the $^4I_{15/2}$ manifold and a crystal field level Y_i in the $^4I_{13/2}$ manifold for a single $^{167}Er^{3+}$ ion in Si. The hyperfine spectra were measured in different magnetic field directions and the identified peak frequencies were used to fit both the Z_1 and Y_i spin Hamiltonians. All four tensors in the spin Hamiltonians are highly anisotropic, with the largest value principal axes in nearly the same direction. The results suggest that the Er^{3+} ion occupies a distorted cubic site with monoclinic (C_1) symmetry. The ZEFOZ fields calculations for this site suggests $^{167}Er^{3+}$ spin coherence times above 1 s could be achieved at ZEFOZ fields of about 1 T in natural Si.

The high field Zeeman splitting spectra show that the splitting between Z_1 and higher levels in the $^4I_{15/2}$ manifold is much larger than 419 GHz (Appendix B). This suggests that the spin Hamiltonian model is valid for the field range considered in locating the ZEFOZ fields. Nevertheless, identification of other crystal-field levels could allow establishing a more sophisticated model with the crystal field theory. The accuracy of the spin Hamiltonian parameters could be improved by introducing an on-chip magnetic field sensor. On the other hand, the high anisotropy of the specific Er site leads to larger uncertainties in the transverse properties of the tensors and, consequently, in the transverse ZEFOZ fields. Smaller fitting uncertainties are expected on cubic or other higher symmetry sites, which can be investigated using the field rotation Zeeman method presented in this paper.

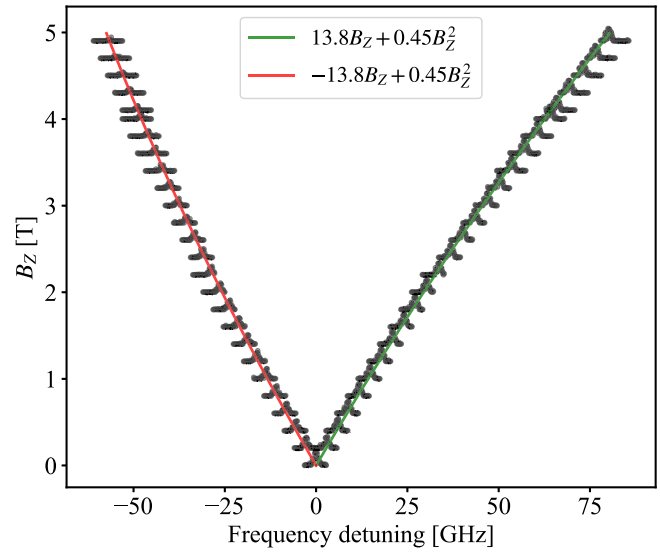

FIG. 6. The Zeeman splitting as a function of magnetic field along the Z axis. The spectra are offset vertically by the corresponding magnetic fields. The solid lines are fittings with linear and quadratic Zeeman shifts.

The data that support the findings of this study are available from the corresponding author upon reasonable request.

ACKNOWLEDGMENTS

The numerical calculations for locating the ZEFOZ fields were performed on the supercomputing system in the Supercomputing Center of University of Science and Technology of China. This work was supported by the National Key R&D Program of China (Grant No. 2018YFA0306600), Anhui Initiative in Quantum Information Technologies (Grant No. AHY050000), and Anhui Provincial Natural Science Foundation (Grant No. 2108085MA15). We acknowledge the AFAiiR node of the NCRIS Heavy Ion Capability for access to ion-implantation facilities.

APPENDIX A: THE TENSORS IN THE CRYSTAL COORDINATE SYSTEM

The three axes X, Y, Z in the laboratory frame are aligned with the crystal directions of [001], [110], [$\bar{1}$10], respectively. As a reference, the fitted tensors in Table II are converted into the following matrices in the crystal coordinate system

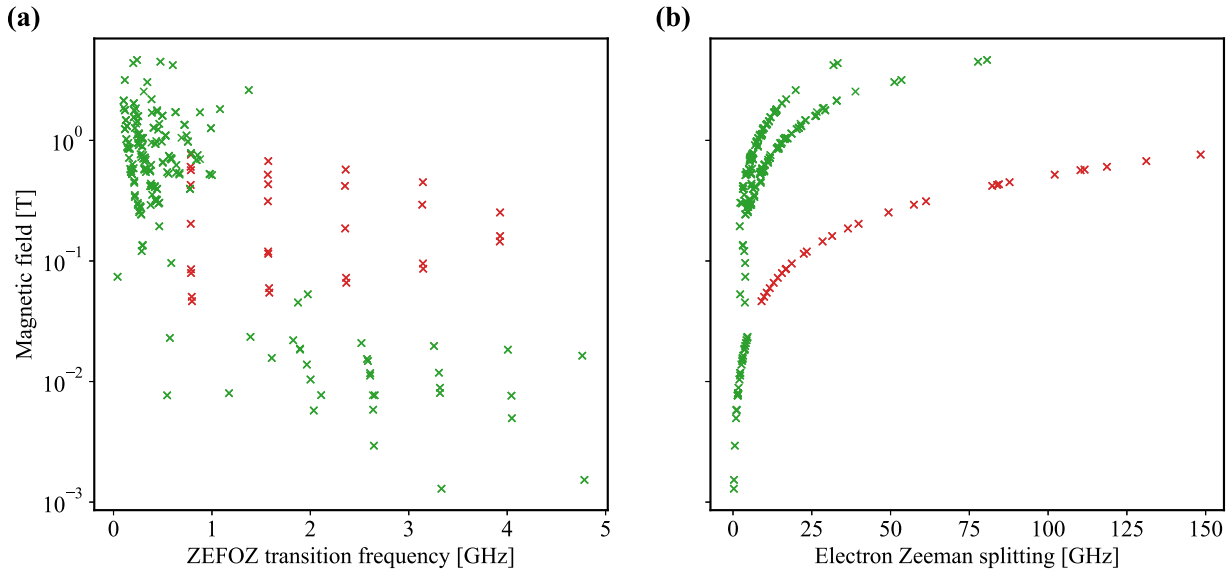

FIG. 7. Field strength versus (a) the transition frequency and (b) the electron Zeeman splitting of the ZEFOZ fields found for the $^{167}Er^{3+}$ ion.

$(\vec{a}, \vec{b}, \vec{c})$, where the three axes are $\vec{a}$ [100], $\vec{b}$ [010], and $\vec{c}$ [001]:

$$\mathbf{g}_{Z_1} = \begin{bmatrix} 3.14 & 0.88 & -5.18 \\ 0.88 & 2.09 & -0.17 \\ -5.18 & -0.17 & 12.54 \end{bmatrix},$$

$$\mathbf{g}_{Y_i} = \begin{bmatrix} 1.33 & -0.17 & -3.86 \\ -0.17 & 0.72 & 1.10 \\ -3.86 & 1.10 & 11.74 \end{bmatrix},$$

$$\mathbf{A}_{Z_1} = \begin{bmatrix} 0.52 & -0.06 & -0.48 \\ -0.06 & 0.32 & -0.08 \\ -0.48 & -0.08 & 1.34 \end{bmatrix} \text{GHz},$$

$$\mathbf{A}_{Y_i} = \begin{bmatrix} 0.68 & -0.12 & -0.54 \\ -0.12 & 0.04 & 0.20 \\ -0.54 & 0.20 & 1.47 \end{bmatrix} \text{GHz}.$$

APPENDIX B: THE HIGH FIELD ZEEMAN SPLITTING SPECTRA

The two-electron spin-preserving transition groups were measured in magnetic fields ranging from 0 to 4.9 T along the Z axis, as shown in Fig. 6. In high fields, the lower frequency branch becomes much weaker while the higher frequency branch becomes stronger, due to the change in the thermal population of the two electron spin states. This indicates that transition b has a higher energy than transition c in a magnetic field along the Z axis, as shown in Fig. 1(a).

The observed nonlinearity can be fitted with linear and quadratic Zeeman shifts, as shown by the solid lines in Fig. 6. We didn't observe higher-order Zeeman shifts or strong bending due to mixing between relatively closely-spaced crystal field levels [27]. This indicates that the Zeeman splitting of the crystal field levels is much smaller than the spacing between the crystal field levels in the magnetic fields considered. At the highest field of $B_Z = 4.9$ T, the electron Zeeman splittings of the Z_1 and Y_i levels are 419 GHz and 280 GHz, respectively. As a result, the spacing between Y_i and $Y_{i\pm1}$ (if it exists) would be much larger than 280 GHz. Also, the observed Z_1 - Y_i transition energy of 195.04 THz matches the typical frequency range for Z_1 - Y_1 transition in Si [7–9]. Therefore, the measured Y_i level is likely to be the Y_1 level for this Er^{3+} site.

APPENDIX C: ADDITIONAL FIGURES OF THE ZEFOZ FIELDS

Figure 7 shows the hyperfine spin transition frequencies and the electron Zeeman splittings at all ZEFOZ fields found for the $^{167}Er^{3+}$ ion. The electron Zeeman splittings are much smaller than the expected crystal field splitting (Appendix B), and therefore the spin Hamiltonian model is valid for the field range considered in locating the ZEFOZ fields.

[1] M. Rančić, M. P. Hedges, R. L. Ahlefeldt, and M. J. Sellars, Coherence time of over a second in a telecom-compatible quantum memory storage material, Nat. Phys. **14**, 50 (2018).

[2] M. Le Dantec, M. Rančić, S. Lin, E. Billaud, V. Ranjan, D. Flanigan, S. Bertaina, T. Chanelière, P. Goldner, A. Erb *et al.*, Twenty-three–millisecond electron spin coherence of erbium ions in a natural-abundance crystal, Sci. Adv. **7**, eabj9786 (2021).

[3] M. Zhong, M. P. Hedges, R. L. Ahlefeldt, J. G. Bartholomew, S. E. Beavan, S. M. Wittig, J. J. Longdell, and M. J. Sellars, Optically addressable nuclear spins in a solid with a six-hour coherence time, Nature (London) **517**, 177 (2015).

[4] A. M. Dibos, M. Raha, C. M. Phenicie, and J. D. Thompson, Atomic Source of Single Photons in the Telecom Band, Phys. Rev. Lett. **120**, 243601 (2018).

[5] S. Chen, M. Raha, C. M. Phenicie, S. Ourari, and J. D. Thompson, Parallel single-shot measurement and coherent control of solid-state spins below the diffraction limit, Science **370**, 592 (2020).

[6] Y.-H. Chen, X. Fernandez-Gonzalvo, S. P. Horvath, J. V. Rakonjac, and J. J. Longdell, Hyperfine interactions of Er^{3+} ions in Y_2SiO_5: Electron paramagnetic resonance in a tunable microwave cavity, Phys. Rev. B **97**, 024419 (2018).

[7] H. Przybylinska, W. Jantsch, Y. Suprun-Belevitch, M. Stepikhova, L. Palmetshofer, G. Hendorfer, A. Kozanecki, R. J. Wilson, and B. J. Sealy, Optically active erbium centers in silicon, Phys. Rev. B **54**, 2532 (1996).

[8] H. Przybylinska, G. Hendorfer, M. Bruckner, L. Palmetshofer, and W. Jantsch, On the local structure of optically active Er centers in Si, Appl. Phys. Lett. **66**, 490 (1995).

[9] Y. S. Tang, K. C. Heasman, W. P. Gillin, and B. J. Sealy, Characteristics of rare-earth element erbium implanted in silicon, Appl. Phys. Lett. **55**, 432 (1989).

[10] U. Wahl, A. Vantomme, J. De Wachter, R. Moons, G. Langouche, J. G. Marques, J. G. Correia, and ISOLDE collaboration, Direct Evidence for Tetrahedral Interstitial Er in Si, Phys. Rev. Lett. **79**, 2069 (1997).

[11] M. Needels, M. Schlüter, and M. Lannoo, Erbium point defects in silicon, Phys. Rev. B **47**, 15533 (1993).

[12] J. Wan, Ye Ling, Q. Sun, and X. Wang, Role of codopant oxygen in erbium-doped silicon, Phys. Rev. B **58**, 10415 (1998).

[13] M. Hashimoto, A. Yanase, H. Harima, and H. Katayama-Yoshida, Detemination of the atomic configuration of Er-O complexes in silicon by the super-cell FLAPW method, Phys. B: Condens. Matter **308**, 378 (2001).

[14] D. Prezzi, T. A. G. Eberlein, R. Jones, J. S. Filhol, J. Coutinho, M. J. Shaw, and P. R. Briddon, Electrical activity of Er and Er-O centers in silicon, Phys. Rev. B **71**, 245203 (2005).

[15] A. G. Raffa and P. Ballone, Equilibrium structure of erbium-oxygen complexes in crystalline silicon, Phys. Rev. B **65**, 121309(R) (2002).

[16] C. Delerue and M. Lannoo, Description of the Trends for Rare-Earth Impurities in Semiconductors, Phys. Rev. Lett. **67**, 3006 (1991).

[17] C. A. J. Ammerlaan and I. de Maat-Gersdorf, Zeeman splitting factor of the Er^{3+} ion in a crystal field, Appl. Magn. Reson. **21**, 13 (2001).

[18] R. K. Watts and W. C. Holton, Paramagnetic-resonance studies of rare-earth impurities in II-VI compounds, Phys. Rev. **173**, 417 (1968).

[19] J. D. Carey, R. C. Barklie, J. F. Donegan, F. Priolo, G. Franzó, and S. Coffa, Electron paramagnetic resonance and photoluminescence study of Er-impurity complexes in Si, Phys. Rev. B **59**, 2773 (1999).

[20] J. D. Carey, State mixing and the cubic crystal field approximation for rare earth ions: The case of the Er^{3+} ion in axial crystal fields, J. Phys.: Condens. Matter **21**, 175601 (2009).

[21] G. Hu, G. G. de Boo, B. C. Johnson, J. C. McCallum, M. J. Sellars, C. Yin, and S. Rogge, Time-resolved photoionization detection of a single Er^{3+} ion in silicon, Nano Lett. **22**, 396 (2022).

[22] L. Weiss, A. Gritsch, B. Merkel, and A. Reiserer, Erbium dopants in nanophotonic silicon waveguides, Optica **8**, 40 (2021).

[23] A. Gritsch, L. Weiss, J. Früh, S. Rinner, and A. Reiserer, Narrow optical transitions in erbium-implanted silicon waveguides, arXiv:2108.05120.

[24] I. Berkman, A. Lyasota, G. de Boo, J. Bartholomew, B. Johnson, J. Mccallum, B.-B. Xu, S. Xie, R. Ahlefeldt, M. Sellars, C. Yin, and S. Rogge, Sub-megahertz homogeneous linewidth for Er in Si via in situ single photon detection, arXiv:2108.07090.

[25] D. L. McAuslan, J. G. Bartholomew, M. J. Sellars, and J. J. Longdell, Reducing decoherence in optical and spin transitions in rare-earth-metal-ion–doped materials, Phys. Rev. A **85**, 032339 (2012).

[26] C. Yin, M. Rancic, G. G. de Boo, N. Stavrias, J. C. McCallum, M. J. Sellars, and S. Rogge, Optical addressing of an individual erbium ion in silicon, Nature (London) **497**, 91 (2013).

[27] G. G. de Boo, C. Yin, M. Rančić, B. C. Johnson, J. C. McCallum, M. J. Sellars, and S. Rogge, High-resolution spectroscopy of individual erbium ions in strong magnetic fields, Phys. Rev. B **102**, 155309 (2020).

[28] Q. Zhang, G. Hu, G. G. de Boo, M. Rančić, B. C. Johnson, J. C. McCallum, J. Du, M. J. Sellars, C. Yin, and S. Rogge, Single rare-earth ions as atomic-scale probes in ultrascaled transistors, Nano Lett. **19**, 5025 (2019).

[29] O. Guillot-Noël, P. Goldner, Y. L. Du, E. Baldit, P. Monnier, and K. Bencheikh, Hyperfine interaction of Er^{3+} ions in Y_2SiO_5: An electron paramagnetic resonance spectroscopy study, Phys. Rev. B **74**, 214409 (2006).

[30] S. P. Horvath, J. V. Rakonjac, Y.-H. Chen, J. J. Longdell, P. Goldner, J. P. R. Wells, and M. F. Reid, Extending Phenomenological Crystal-Field Methods to C_1 Point-Group Symmetry: Characterization of the Optically Excited Hyperfine Structure of $^{167}Er^{3+}:Y_2SiO_5$, Phys. Rev. Lett. **123**, 057401 (2019).

[31] A. Högele, S. Seidl, M. Kroner, K. Karrai, C. Schulhauser, O. Sqalli, J. Scrimgeour, and R. J. Warburton, Fiber-based confocal microscope for cryogenic spectroscopy, Rev. Sci. Instrum. **79**, 023709 (2008).

[32] H. Sellier, G. P. Lansbergen, J. Caro, S. Rogge, N. Collaert, I. Ferain, M. Jurczak, and S. Biesemans, Subthreshold channels at the edges of nanoscale triple-gate silicon transistors, Appl. Phys. Lett. **90**, 073502 (2007).

[33] See Supplemental Material at http://link.aps.org/supplemental/10.1103/PhysRevB.105.235306 for 3D animations of Figs. 2(a) and 5.

[34] J. Yang, J. Wang, W. Fan, Y. Zhang, C. Duan, G. Hu, G. G. de Boo, B. C. Johnson, J. C. McCallum, S. Rogge, C. Yin, and J. Du, Spectral broadening of a single Er^{3+} ion in a Si nanotransistor, arXiv:2201.11472.

[35] E. Fraval, Minimising the decoherence of rare earth ion solid state spin qubits, Ph.D. thesis, Research School of Physical Sciences and Engineering and The Australian National University, 2005.

[36] T. Böttger, C. W. Thiel, Y. Sun, and R. L. Cone, Optical decoherence and spectral diffusion at 1.5 μm in $Er^{3+}:Y_2SiO_5$ versus magnetic field, temperature, and Er^{3+} concentration, Phys. Rev. B **73**, 075101 (2006).

[37] O. Guillot-Noël, H. Vezin, P. Goldner, F. Beaudoux, J. Vincent, J. Lejay, and I. Lorgeré, Direct observation of rare-earth-host interactions in $Er:Y_2SiO_5$, Phys. Rev. B **76**, 180408(R) (2007).